Physics of Fluids

Influence of wetting behavior on the morphology of droplet impacts onto dry smooth surfaces

Cite as: Phys. Fluids **33**, 063305 (2021); https://doi.org/10.1063/5.0053539
Submitted: 08 April 2021 • Accepted: 14 May 2021 • Published Online: 03 June 2021

P. Foltyn, D. Ribeiro, A. Silva, et al.

Physics of Fluids ARTICLE scitation.org/journal/phf

Influence of wetting behavior on the morphology of droplet impacts onto dry smooth surfaces

Cite as: Phys. Fluids **33**, 063305 (2021); doi: 10.1063/5.0053539
Submitted: 8 April 2021 · Accepted: 14 May 2021 ·
Published Online: 3 June 2021

P. Foltyn,[1,a)] D. Ribeiro,[2] A. Silva,[2] G. Lamanna,[1] and B. Weigand[1]

AFFILIATIONS

[1]Institute of Aerospace Thermodynamics, University of Stuttgart, 70569 Stuttgart, Germany
[2]AEROG-LAETA, University of Beira Interior, 6201-001 Covilhã, Portugal

[a)]Author to whom correspondence should be addressed: patrick.foltyn@itlr.uni-stuttgart.de

ABSTRACT

The influence of wettability on the morphology of droplet impacts onto dry surfaces is often neglected in the literature, despite its significant effect on the resulting morphology. In this work, the role of wettability is investigated systematically by considering droplet impact processes on smooth dry surfaces of two different materials. The wetting behavior is varied not only by employing two different fluids, but most importantly by varying the surface properties by plasma activation and polymerization. Overall, this leads to four different wetting behaviors for each surface. The changes in impact morphology are visualized by means of a three-perspective experimental facility. In particular, the bottom view employs a total internal reflection-configuration for visualizing the exact droplet contact area and contact time. This enables us to characterize the main features of the different wetting behaviors. Overall, we found that surface wettability mainly influences the receding phase, resulting in higher receding rates with decreasing wettability but also the maximum spreading diameter.

I. INTRODUCTION

A droplet impinging on a solid surface is a common and well-known event, which is of relevance in several applications: soil erosion, fire suppression, fuel injection in internal combustion engines, spray cooling, spray coating, spray painting, just to name a few.[1] Typically, different outcomes can be expected from a single droplet impinging on a dry solid substrate, namely, deposition, crown splash, and prompt splash.[2] Changing the surface wettability will, in general, not affect the above classification, but it will influence significantly the overall dynamics of the lamella's spreading by inducing breakup, as well as full or partial rebound. Hereby, the surface wettability is used as a characterizing parameter, which is the ability of a fluid to spread out on a dry solid substrate and it is quantified by the apparent contact angle θ_{app}.[1] A detailed physical description will be given in Sec. II A. Different contact angles define different wettability behaviors, which can be fully wettable, partially wettable, or nonwettable. The effect of wettability is a key parameter on the outcome of droplet impacts. On fully wetting surfaces, a thin liquid film forms leading to an increase in heat transfer between the droplet and the wall or to self-cleaning properties,[3,4] especially for porous surfaces or surfaces with a large spectrum of different (hierarchical) structures. On the other hand, low-wetting surfaces, which can be generated, e.g., by roughness, are widely known as "repelling surfaces." Their wide range of applications is often related to the underlying self-cleaning mechanism often called the "Lotus effect." Understanding the physical mechanisms of wetting transition is essential for the design of efficient functional surfaces and materials.[5]

Up to now, the role of surface characteristics on the dynamic behavior of droplets impinging on a dry surface is not fully understood. Wettability is an equilibrium thermodynamic variable that depends exclusively on the interfacial free surface energies of the surface, according to Young's law.[6] The equilibrium is reached very fast, but the contact angle is a dynamic parameter and an interdependency between the spreading behavior and the dynamic contact angle can be found.[7] As an example, experiments have shown that the dynamic contact angle depends on the spreading rate, which, however, influences the dynamic contact angle again.[8]

The formation of complete or full wetting ($\theta_{app} = 0°$) possibly happens due to the presence of a precursor film on the surface, providing faster spreading rates since it leads to a force acting in the direction of spreading promoting further surface wetting. This phenomenon causes superspreading behavior and inhibits the characterization of the liquid-surface system using the equilibrium contact angle.

In 1997, Mao *et al.*[9] varied the equilibrium contact angle and did not observe changes in the maximum spreading diameter for

impacting droplets. Later in 2002, Rioboo *et al.*[10] studied the role of surface wettability on the droplet spreading and observed differences in the final stages of spreading, for nonwettable surfaces. This is supported by the results of Moita and Moreira[11] who show that a decreasing contact angle increases the spreading rate. It should not be forgotten that in these experiments, very low impact velocities were considered, where the wettability effects may be more noticeable. According to Pasandideh-Fard *et al.*,[12] wettability may be negligible for high Weber numbers but seems to be significant for low impact velocities. Even if wettability may be negligible in some cases, the contact angles seem to be important in the spreading and receding mechanisms,[13] which must not be forgotten in modeling. The spreading characteristics are the most studied features related to wettability, but a question arises: How exactly does wettability influence the outcome of a single droplet impinging on a dry surface? Additionally, what phenomena could be expected depending on the wettability and how do they evolve?

The variation in wetting behavior was usually achieved by droplet impacts on different surface materials. Thus, surface materials, wettability, and the characteristic roughness, even if it is in nanometric scale, were always exchanged as a complete set.[13–15] In opposition to that, a systematic study of droplet impacts onto dry solid surfaces is presented at which the surface wettability has been flexibly controlled by plasma activation and plasma polymerization. With this approach, it could be set in a range from full wetting to nonwetting while not exchanging the used polymeric materials or surfaces. Further subject of systematic changes had been the droplet fluid, surface materials, and impact energy resulting into the impact condition range of $80 < We < 1165$ and $1135 < Re < 12\,240$. The experimental facility is introduced in detail and has three synchronized perspectives (lateral, top, and bottom) using high-speed imaging. The bottom perspective is a unique feature of the optical setup, which gives insight into interesting phenomena like bubble entrapment at the impact point.[16–19]

II. EXPERIMENTAL METHODS

In Secs. II A–II C, information are given regarding the physical background, the droplet impact facility, which includes three synchronized perspectives, and the plasma treatments applied on the surface samples to modify the wettability.

A. Definition, estimation, and measurement of contact angles

The wetting capability of a liquid can be characterized by the formed apparent contact angle θ_{app}. In this publication, we follow the definition of Marmur *et al.*[20] The apparent contact angle is defined as the angle on the liquid side between the tangent of the solid surface and the tangent of the liquid–vapor phase, see Fig. 1(a). The abilities of wetting can be classified into different classes with respect to the observable apparent contact angle. Wettable surfaces, forming apparent contact angles $\theta_{app} < 90°$, are considered as "hygrophilic." For $\theta_{app} > 90°$, the surface is nonwettable, called "hygrophobic." There are also two extreme cases: for $\theta_{app} \approx 0°$, the surface is fully wettable, called "superhygrophilic," and for $\theta_{app} > 150°$, the surface is "superhygrophobic." The "hygro" stands for liquids in general while "hydro" is often used but it is only valid in the case of water. As explained in Ref. 20, the measured apparent contact angle might

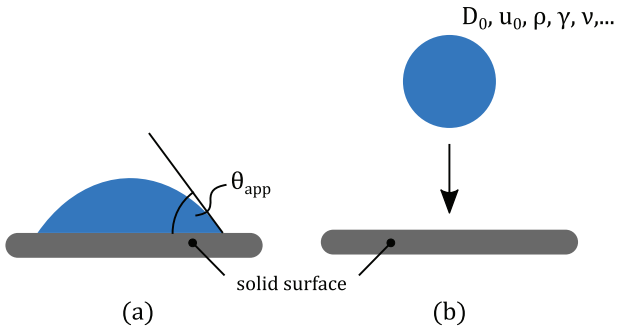

FIG. 1. Definition of (a) the apparent contact angle θ_{app} and (b) the impact conditions.

deviate from the equilibrium Young-contact angle θ_Y, described as follows:[6]

$$\gamma_S - \gamma_{SL} = \gamma_L \cos\theta_Y. \tag{1}$$

The Young-contact angle θ_Y is thermodynamically stable since it has the lowest Gibbs-energy. It can be estimated using the free surface energies of the solid γ_S, the solid–liquid γ_{SL}, and the liquid interface γ_L. However, the estimation of γ_{SL} is difficult to obtain. Therefore, the prediction with the help of the method of Owens, Wendt, Rabel, and Kaelble (OWRK-model)[21–23] is used. Herein, the surface free energies are split into polar and dispersive parts,[24]

$$\gamma_i = \gamma_i^p + \gamma_i^d, \tag{2}$$

and the solid–liquid interfacial energy γ_{SL} can be expressed with the help of Eq. (2) as follows:

$$\gamma_{SL} = \gamma_S + \gamma_L - 2\left(\sqrt{\gamma_S^p\gamma_L^p} + \sqrt{\gamma_S^d\gamma_L^d}\right). \tag{3}$$

The prediction of the contact angle can be then done using the following equation, which is obtained by inserting Eqs. (2) and (3) into the Young-equation (1):

$$\cos(\theta_{OWRK}) = 2/\gamma_L\left(\sqrt{\gamma_S^p\gamma_L^p} + \sqrt{\gamma_S^d\gamma_L^d}\right) - 1. \tag{4}$$

The measurement of θ_{app} is done by the sessile drop method using an optical contour analysis (OCA) system manufactured by *DataPhysics Instruments GmbH*. The measurement procedure is as follows. First, the surface sample on which the apparent contact angle needs to be measured is placed on a height-adjustable platform. Second, the droplet is produced by using a precise pump delivering a volume of 5 μL so that the droplet is hanging on the needle tip. As liquids, distilled water and isopropanol are used, which are from the same material batch, which is used later in the experiments. Third, the height of the height-adjustable platform is increased to pickup very slowly the hanging droplet in order to maintain a very low relative velocity between the droplet and the surface sample. Fourth, diffuse backlight images are acquired, the baseline is manually defined, and an elliptical fit is used for fitting the contour of the droplet shape. Finally, the arithmetic mean value of the contact angle at both triple points is used as the apparent contact angle. In order to maintain consistency

and to minimize the influence of inhomogeneous free surface energy distributions, the whole procedure is repeated while the measurement spots are randomly distributed. The arithmetic mean of the gathered θ_{app} is then taken as a reference value for these surface samples and the following evaluations.

The calculated contact angle θ_{OWRK} for water on polycarbonate (Lexan®, PC) using Eq. (4) gives a value of $\theta_{OWRK} \approx 79.9°$ while the OCA measurement gives $\theta_{app} \approx 79.8°$. For the free surface energies of water,[25] $\gamma_{LV}^{p} = 51.00\ \mathrm{mN\,m^{-1}}$ and $\gamma_{LV}^{d} = 21.80\ \mathrm{mN\,m^{-1}}$ are used and for PC the free surface energies[26] $\gamma_{SV}^{p} = 6.5\ \mathrm{mN\,m^{-1}}$ and $\gamma_{SV}^{d} = 27.7\ \mathrm{mN\,m^{-1}}$ are used. For Plexiglas® [poly(methyl methacrylate), PMMA], analogous results can be obtained. Therefore, the deviation between θ_Y or θ_{OWRK}, respectively, and θ_{app} is not considered as significantly high for the used smooth polymeric surface samples and the critical remarks in Ref. 27 about the applicability of such models are not significant for the used cases. As a result, the measured θ_{app} is used as a reference angle to identify the general wetting behavior of the sample.

B. Droplet impact facility

The droplet impacts on surface samples with various wetting behaviors have been investigated by a three-perspective experimental test rig using high-speed cameras. The surface samples are placed on a prism, which is the sample holder and one of the key optical elements of the test rig. The impact point is indicated by the origin of the coordinate system in Fig. 2. The test rig consists mainly of three different units, the droplet generation unit, the triggering and synchronization unit, and the image acquisition unit, which are described in Sec. II B 1.

1. Droplet generation unit

For generating single droplets, a blunt needle with an outer diameter of 0.4 mm is used. The impact velocity is set by increasing the falling height of the droplet. Falling heights of 0.15, 0.35, 0.70, and 1.30 m were chosen resulting in four different impact conditions for each liquid, see Tables I and II. For the two higher heights, the impact region of the droplet was strongly influenced by the detachment process at the needle. Therefore, tilting the needle by approximately 45° to one side ensures that the droplet detachment always occurs at the same position of the needle and the falling trajectory is more deterministic. The needle was fed by a medical syringe pump, which was continuously pumping liquid from a glass syringe through a Teflon®-pipe to

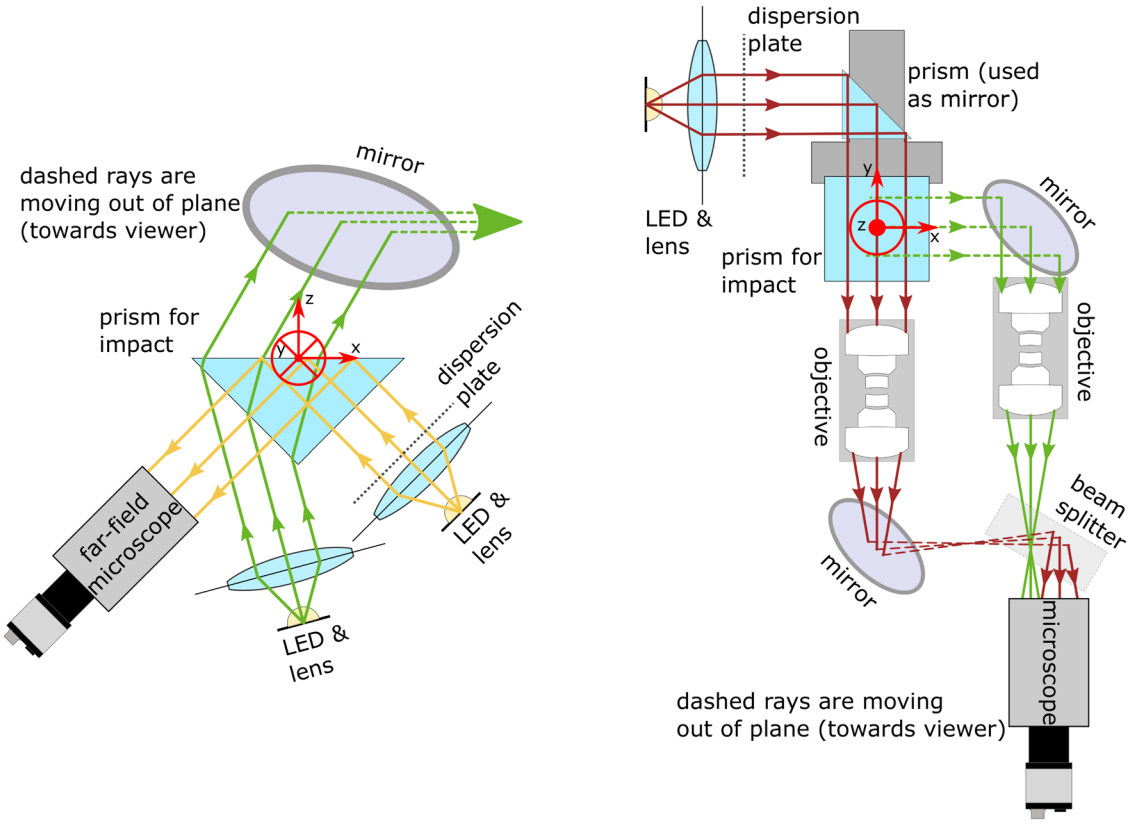

FIG. 2. Schematic sketch of the droplet impact facility's optical concept: (a) front view and (b) top view. Each light path is indicated by a separate color. Dashed rays emerge from the sketch plane. The origin of the test rig coordinate system, marked with a red cross, is set at the impact point.

TABLE I. Summary of the evaluated parameters. For each column, the indicated parameter range was investigated. The parameters which require a pretreatment by plasma activation or polymerization are marked.

Liquid		Distilled water				Isopropanol (2-propanol)			
Material		PC		PMMA		PC		PMMA	
Contact angle		0°*		0°*		0°		0°	
		25° to 40°*		25° to 40°*					
		79.8°		75.1°		66° to 73°*		66° to 73°*	
		117° to 122°*		117° to 122°*					
Impact height		0.15 m	0.35 m	0.70 m	1.30 m	0.15 m	0.35 m	0.70 m	1.30 m
Impact conditions	Re:	4130	6860	9360	12 240	1135	1745	2315	2955
	We:	80	205	385	665	165	400	715	1165
Surface structure		smooth				smooth			
Plasma treatments		The used samples were treated by plasma activation (*) and plasma polymerization (*)							

TABLE II. Physical properties of the used fluids for the experimental study at an ambient temperature of 25 °C.

	Unit	Distilled water	Isopropanol (2-propanol)	References
Density ρ	kg m^{-3}	997.1	781.5	28,29
Dyn. viscosity μ	mPa·s	0.8897	2.045	30,31
Surface tension γ	N m^{-1}	0.071 98	0.020 92	32,33

the needle at a moderate flow rate of 0.5 ml/min. Glass and Teflon were chosen as a tubing material to avoid any chemical incompatibilities and alterations of the liquid during the pumping process. The parts that are not made of glass and Teflon are medical equipment. Therefore, and also due to the very short passages, the liquid is passing nonglass- or non-Teflon-material, and the influence onto the chemical consistency of the droplet liquid is neglected. A one-way valve is employed to avoid back-flow inside the pump, pipes, and needle, which might lead to the formation of air bubbles. The latter also guarantees a continuous flow and a homogeneous detachment of the droplets with constant droplet sizes at a rate of approximately 1.5 Hz. For one impact experiment, one droplet of the droplet chain was selected to pass a barrier while the rest of the droplets were sorted out.

2. Triggering and synchronization unit

The falling droplet passes a LASER light barrier, which provides a 5V Transistor-Transistor-Logic (TTL)-signal when the droplet is cutting the light sheet. The TTL-signal is passed to the cameras starting the image acquisition unit and to an oscilloscope for checking the time synchronization. Top and lateral perspectives are automatically synchronized since both perspectives share one common CMOS-chip of a *Photron SA-X2* high-speed camera, see Secs. II B 3 b and II B 3 c and Fig. 2 for further details. The bottom perspective is synchronized with the other two perspectives as well. This is achieved by setting one of the two high-speed cameras as "primary" and the other as "replica" camera. The primary camera receives the TTL-signal of the LASER light barrier first and passes this to the replica with a shutter time of 1/88 888 s and the frame rate of 20 000 fps. As a result, the images of both cameras have no measurable temporal shift between each other during the acquisition, which is constantly cross-checked by the used oscilloscope at a sampling rate of 125 kHz for each channel.

3. Image acquisition unit

The image acquisition unit records three perspectives: the bottom, top, and lateral perspective. A sketch of the image acquisition unit is depicted in Fig. 2 in which the light paths of the different perspectives are marked in different colors. All three are used for a detailed evaluation of the droplet phenomena, namely, deposition, prompt splash, crown splash, receding breakup, partial rebound, and complete rebound, as reported in the literature.[1,2,34,35] The resolution was set to 1024 × 672 px^2 for both cameras. Due to the different perspectives, each image is individually corrected to eliminate any perspective distortion before any further evaluation is made. A detailed description of the respective perspectives follows.

a. Bottom perspective. The motivation of not using only a lateral perspective is that the partial shadowing of the bottom perspective is widely common to understand the complexity of the pattern of fine flows created, e.g., by the splashing of a droplet on a steady liquid film.[36,37] However, with the help of a total internal reflection configuration, one can even distinguish between wetted and dry areas for droplet impact onto dry smooth surfaces, which is marked in Fig. 2(a) as a yellow light path. In Fig. 3, the principle of the total internal reflection configuration is illustrated.

Parallel light coming from a white LED and a lens enters the prism with an angle of 45° related to the top surface, see Figs. 2(a) and 3(a). The dispersion plate is used to obtain a more homogeneous light distribution in the image. The total internal reflection occurs on the

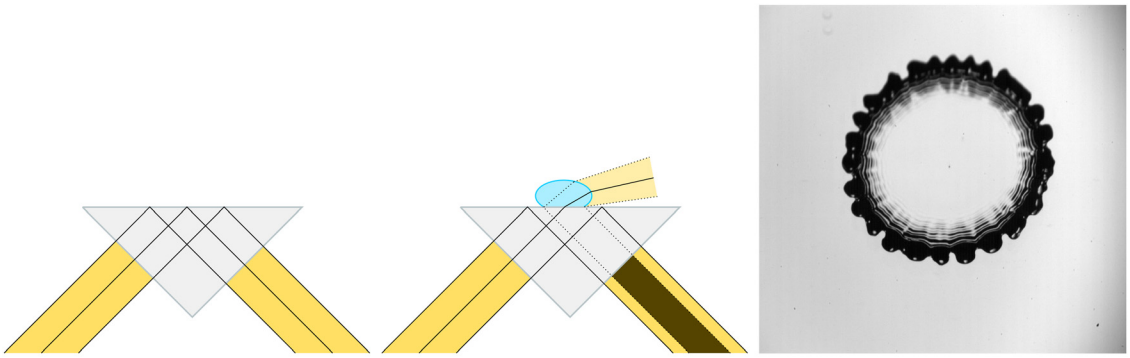

FIG. 3. Principle of the total internal reflection configuration: (a) dry surface on which all light rays are reflected; (b) wetted surface with curved profile leads to partial diffraction of light exiting to the top-side of the prism; and (c) perspective-corrected image from experimental campaign showing the dry and wetted areas of the surface. The middle of the droplet is also wetted, however, due to the horizontal droplet lamella the total internal reflection condition is met again.

top surface and the reflected light is exiting the prism and entering a far-field microscope mounted to the high-speed camera. The microscope is focused on the spot where the droplet is impacting on the surface, indicated by a red cross in Fig. 2(a).

The critical angle ξ_{crit}, which is the minimum angle of the incident ray, for a total reflection can be calculated by Snell's Law.[38] According to Eq. (5), it is only depending on the ratio of the refractive indices of the adjacent media at the interface n_i/n_j,

$$n_1 \sin \xi_1 = n_2 \sin \xi_2, \tag{5}$$

$$\xi_{crit} = \arcsin n_2/n_1. \tag{6}$$

For the combination glass prism, made of N-BK7 ($n_1 = 1.514$ at 680 nm)[39] and air ($n_2 \approx 1$ at 680 nm),[40] the critical angle according to Eq. (6) gives $\xi_{crit} \approx 41.3°$. The wavelength of 680 nm is used as reference due to the maximum quantum efficiency for the *Photron SA-X2* high-speed cameras.[41] If the top-side of the prism is wetted, compare Figs. 3(a) and 3(b), the relation of the refractive indices, specifically n_2, is changing leading locally to light diffraction and not to total internal reflection. These areas cause dark spots on the camera, see Figs. 3(b) and 3(c). An exception is if the wetted area has again a horizontal surface. Then the total internal reflection occurs again. However, the boundary of such areas is not horizontal and, therefore, surrounded by a black area so that there is a definite assignment of the wetted and nonwetted areas possible. An exemplary sequence of a droplet impact seen from the bottom perspective can be found at the bottom row of the sequences in Fig. 8.

b. Top perspective. Similar to the bottom perspective, parallel light for the diffuse backlight images of the top view is generated, by using a white LED and a lens. The light enters the prism and leaves it at a certain angle after being refracted twice at the two interfaces, see the green ray path in Fig. 2(a). In order to minimize the offset of the light path into the x-direction, the light source is rotated by a small angle. The diffuse backlight image of the droplet impact is then projected onto a mirror, which is stopping the shift in the x-direction. This shift into the x-direction is due to the prism and is unavoidable. The rays are then reflected by the mirror orthogonally in −y-direction to the microscope, see Figs. 2(a) and 2(b). The high-speed camera is mounted to a *WILD Heerbrugg M8 Zoom stereomicroscope*. It can provide a magnification range of 1× to 40×. However, the working distance of the microscope is approximately 90 mm, which is far too low to be able to make a combined observation of the droplet impact for both perspectives. Therefore, an intermediate imaging for each perspective needs to be realized using, in total, two *Schneider Kreuznach Symmar 80/5.6* objectives. The optical path between the droplet impact area and the microscope is then enlarged by additional approximately 320 mm. This enables a shared CMOS-Chip with the arrangement of all optical equipment in a proper and feasible manner. After passing the objective, the rays are transmitted to a 50:50 beam splitter plate before they enter the microscope. Since the beam splitter serves also as a mirror for the other ray path from the lateral perspective, it is used to finally combine both images on one CMOS-chip. An example of the top perspective can be seen in the middle row of each image sequence in Fig. 8.

c. Lateral perspective. For the lateral perspective, indicated in red, the light is again created by a white LED, a lens, and a dispersion plate, see Fig. 2(b). Due to the test rig periphery, it has to be reflected for 90° by a small prism. The light then traverses the area of the droplet impact and is used for a diffuse backlight image. Again, a *Schneider Kreuznach Symmar 80/5.6* objective is used for the intermediate image to enlarge the optical distance between the impact area and the microscope. In order to place the lateral view next to the top view on the beam splitter, a shift of the lateral view in x- and z-direction is required. For this purpose, a mirror is used to redirect the rays diagonally upwards, see Fig. 2(b). The beam splitter plate serves as a mirror for this perspective and reflects the rays inside the microscope onto the CMOS-chip of the camera. The top row of each sequence in Fig. 8 shows the lateral perspective of an impacting droplet on a surface.

C. Plasma treatment of surface samples

The polymeric surface samples have been plasma treated in order to manipulate the wetting behavior of the liquid–solid combination. For this purpose, two different plasma machines of the type *FEMTO*,

manufactured by *Diener electronic GmbH & Co KG*, were used. Low-pressure plasma activation was used to promote the wetting behavior for water on the polymers. Plasma polymerization was used to apply a very thin, nanometric coating to the surface in order to decrease the wetting behavior and increase the contact angle, respectively. For the experimental campaign, all surface samples for one data row with the same contact angle have been plasma treated together. Additionally, some spare samples were also included in this batch to measure the reference contact angle as explained in Sec. II A, which will be then used for further evaluations.

In the literature,[13,15,42] there are several studies about the influence of surface wettability onto the droplet impact morphology. The wettability has been changed due to coating or due to the usage of different surface materials. With the help of the plasma treatments, the surface wettability can be changed without exchanging those surface materials and the characteristic surface roughness stays constant.

1. Plasma activation

During the activation, some groups of the atomic structure of the polymer are substituted by free radicals, like peroxide groups due to the oxygen inside the air. Substitutions with peroxide groups enhance the polar part and might even decrease the dispersive part to the surface free energy.[43] In using Eq. (4), the resulting contact angles might be even predicted, if required. The activation process itself is mainly dependent on the activation duration, the discharge current, the used gas, and the gas pressure.[43] For our case, ambient air was used at a pressure of (155 ± 5) μbar. This pressure was chosen since the plasma showed no major changes in distribution and strength inside the chamber in a range between 100 and 200 μbar. In addition to the activation duration, all other parameters were kept constant so that only the duration was controlling the desired apparent contact angles θ_{app} as summarized for the different surface materials and cases in Table I.

2. Plasma polymerization

The plasma polymerization is forming high-molecular products from initially low-molecular substances, e.g., monomers.[43] The formation occurs in nonthermal plasma using a pressure of approximately 10 Pa. All process parameters, e.g., generator power, pressure, mass flow of the monomer, temperature, and the process duration, are fully controlled by a PC system based on Windows® 7 Embedded. The initial low-molecular substance was a perfluor-monomer, which is distributed directly by the manufacturer of the plasma machines. The monomer forms a "Teflon-like" coating which is not interfering with the optical setup. As provided in Table I, the contact angles could be significantly increased in comparison to the untreated surfaces. According to the distributor, water droplets on smooth, well-polymerized surfaces can achieve contact angles of approximately 120°. Thus, it can be also stated that the surfaces were always successfully treated.

III. EXPERIMENTAL APPROACH

A. The investigated parameter space

The investigated parameters are summarized in Table I. In total, two different surface materials, namely, Lexan (PC) and Plexiglas (PMMA), have been used for droplet impacts. Distilled water and isopropanol (2-propanol) have been used as liquids at an ambient temperature of 25 °C. Their physical properties are summarized in Table II. The diameter of the impacting droplet was set to (2.3 ± 0.1) mm and (1.9 ± 0.1) mm, respectively. For distilled water, four different wetting behaviors have been investigated, while for isopropanol only two. The reason is that the natural apparent contact angle θ_{app} for water on PC and PMMA is 79.8° and 75.1°, respectively, while for isopropanol the angle is for both materials 0°. Therefore, no further increasing wettability of isopropanol could be achieved using plasma activation. For distilled water, two different increased wetting behaviors have been investigated, using plasma activation. First, the samples were fully activated, so that $\theta_{app} \approx 0°$ corresponding to an angle which is too flat to be measured. Second, the resulting contact angles of a very short plasma activation in a range of $\theta_{app} \in [25° - 40°]$ have been used for the experiments. The apparent contact angles θ_{app} larger than the natural one are created by plasma polymerization. For both liquids, four different impact conditions have been used, achieved by four different droplet falling heights, resulting in four pairs of Reynolds and Weber numbers. Both are defined as follows:[44] using the droplet diameter D_0 as the characteristic length, its impact velocity u_0, the surface tension γ, and the droplets density ρ and viscosity μ, see also Fig. 1(b),

$$Re = \frac{\rho u_0 D_0}{\mu}, \tag{7}$$

$$We = \frac{\rho u_0^2 D_0}{\gamma}. \tag{8}$$

B. Experimental procedure

Prior to an experimental campaign, the surface samples need to be prepared. For this, at first, a special and unique pattern is cut in the outer edges of the approximately $2.5 \times 10^{-2} \times 3.0 \times 10^{-2}$ m^2 surface samples. This ensures that the orientation of the surface sample will always be the same. A flipping of the surface sample to the other side, for any reason, can be recognized and corrected. In particular, for the plasma treated surface samples, this is a very important feature since only the upper side of the surface samples is reliably treated in the machines. Second, the surface samples are treated by the respective plasma processes if required by the investigated parameters. After the plasma treatment, one sample is used as a reference sample in order to determine the wetting behavior, see Table I. With the prepared samples, the actual experiment is then performed. At first, all samples are brushed carrying away all dust particles with a *PFA Nitrogen Gun* by *Parker Hannifin Corporation* using high purity (99.999%) nitrogen. Nitrogen has been chosen to avoid any influence of the used gas with the polymer surface. Third, an isopropanol film is applied with a syringe onto the main glass prism which is serving as a coupling medium to ensure that the total internal reflection occurs inside the polymer surface and not in the prism. The isopropanol also helps us to keep the surface sample at one defined place due to the small adhesive forces of the thin liquid film. However, it is important to ensure that no air bubbles will remain between the polymer sample and the glass prism, since this will disturb the images of the bottom perspective. Fourth, after placing and aligning of the surface sample, the cameras are set awaiting the trigger for the acquisition. Finally, the droplet stream has started to generate a homogeneous droplet chain. As soon as the droplets have a uniform size, as well as a reproducible

detachment of the tilted needle tip is determinable, one droplet is allowed to pass the droplet barrier to fall into the test section onto the surface sample. In the moment of passing the light barrier, a trigger signal is sent to all the cameras.

C. Image processing and evaluation

Before the evaluation of the acquired images could start, a multi-step image processing routine was used in order to gather the parameters presented below. The images are processed in three-dimensional stacks having the geometric coordinates x and y of the image as well as a t-coordinate representing the time. At first, for each separate perspective, the respective perspective correction procedure is performed applying transformation matrices and bicubic interpolation. Second, the background is subtracted, the images are split for the top and lateral perspective due to the shared CMOS-chip, see Sec. II B, and the images are binarized applying Otsu's method[45] to the global set of images. After a filtering and cleaning procedure, as well as the determination of the impact frame, which is considered as a time reference point ($t = 0$), the impact parameters are found by tracking the droplets. The droplet impact diameter D_0 is considered as the area-equal diameter which can be calculated using the averaged droplet area A_{avg} using 10 images before the impact corresponding to an averaging time of $\Delta t_{avg} = 0.5$ ms as follows:

$$D_0 = \sqrt{(4A_{avg}/\pi)}. \tag{9}$$

The droplet impact velocity u_0 is averaged for the same 10 images and can be found by tracking the position of the binary droplet centroid X over time and applying the formula

$$u_0 = \sqrt{((X_i - X_{i-1})^2)}/(\Delta t). \tag{10}$$

The time Δt corresponds to the inverse of the camera frame rate (20 000 fps). The later presented spreading diameter D_{spread} is extracted from the bottom perspective applying Eq. (9) again.

IV. RESULTS

In this section, the role of wettability is analyzed in detail with respect to its effect on the splashing limits and the morphology of the impact in the spreading and receding phase.

A. Deposition/splashing limit

Four impact energies were tested to assess also the influence of impact energy on the phenomena morphology obtained. A wide range of impact conditions provides the possibility to establish a comparison between them.

Considering the complete parameter space, three main phenomena were identified: deposition, splashing, and rebound. Figure 4 shows the occurrence of each phenomenon as a function of Reynolds number Re, Weber number We, and apparent contact angle θ_{app}. The phenomena are identified by different colors and symbols. The splashing regime includes both prompt and crown splash and the rebound regime includes both partial and complete rebound. However, Fig. 4 only gives an overview of the outcomes. In order to assess the agreement of our results with the empirical correlations in the literature, different splashing limits were considered.

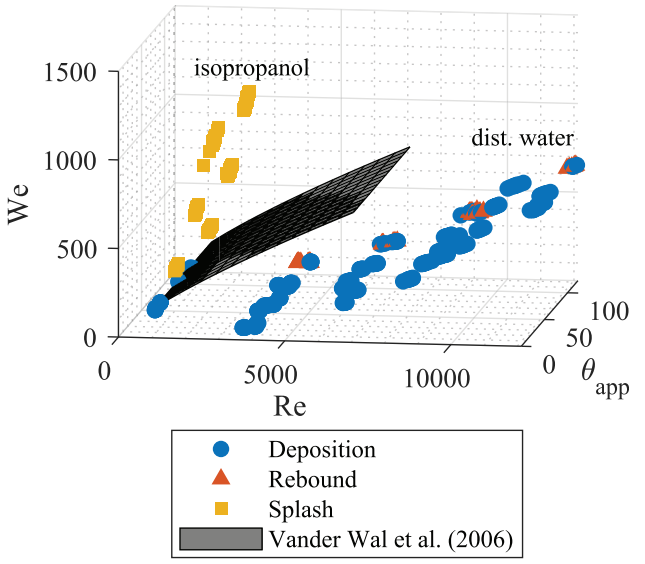

FIG. 4. Regime map of all conducted experiments indicating the found morphologies "deposition," "splashing," and "rebound" as well as the deposition/splashing limit by Vander Wal *et al.*[46]

The well-known criterion developed by Bai and Gosman[47] and the splashing limit developed by Mundo *et al.*[48] had not been applicable, since their validity range did not fit our results. Nonetheless, a splashing limit was developed by Vander Wal *et al.*[46] for the impact of single droplets onto dry surfaces with a mean surface roughness under 10 nm and a validity range of $0 < Re < 7500$, which mostly fits our data. Their splashing limit is described by the following equation, where Oh is the Ohnesorge number, $Oh = \sqrt{We}/Re$:

$$K_c = OhRe^{0.609} = 0.85. \tag{11}$$

Their study is very detailed, using many fluids including alkanes, alcohols, de-ionized water, and glycerol–water solutions, providing a wide range of fluid physical properties. The droplets impinged onto a dry aluminum plate. This plate is fully wettable for the hydrocarbon fluids while for water forms an apparent contact angle of $\theta_{app} = 30°$. In this way, that correlation was added to Fig. 4 as a gray plane. Thus, this correlation fits our results. The outcomes of the isopropanol droplets at low impact velocities, where only deposition was recorded, are very close to the boundary between the regimes. This shows us that the experimental parameters were close to the splashing limit.

In summary, we consider that the Vander Wal *et al.*[46] correlation is suitable for the parameter space of this study and predicts correctly the expected outcomes. The wettability does not influence the splashing limit since splash formation occurs during a fast spreading rate. Thus, the dynamic contact angle can be approximately considered to be 180° due to the high spreading velocity.[7,8] On the other hand, the surface wettability has a significant influence on the receding movement which is relevant for the rebound morphology.

B. Detailed evaluation of droplet spreading

As known from the literature,[15,42] surface wettability does not play a significant role on the outcome regime which is also confirmed

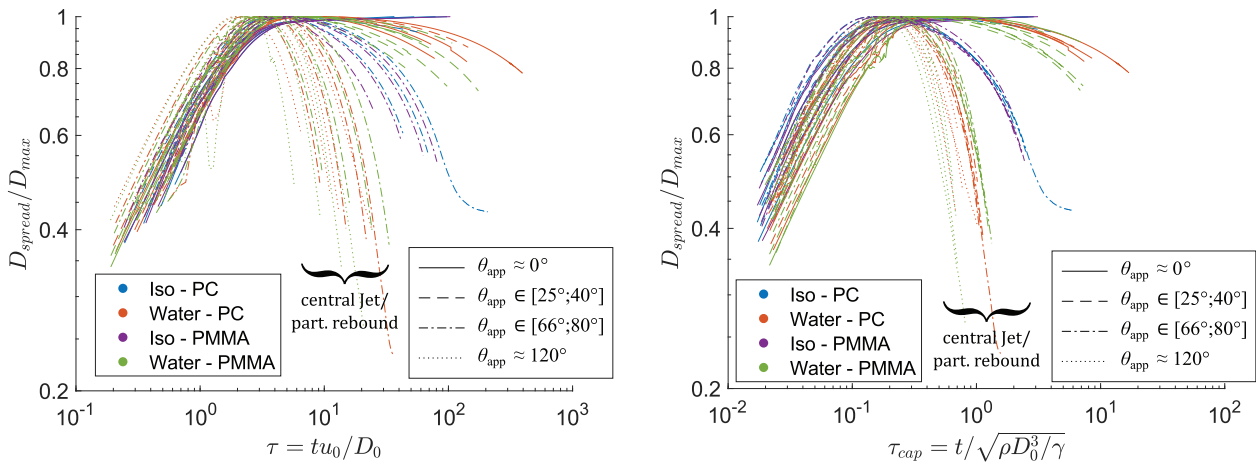

FIG. 5. Spreading diameter D_{spread} normalized with maximum spreading diameter D_{max} vs (a) the dimensionless (inertial) time τ and (b) the dimensionless (capillary) time τ_{cap}.

by the present experiments. However, it does matter on the detailed physical processes during the spreading and receding phases, which are then leading to a certain impact regime.[13] The effect of surface wettability on the spreading and receding behavior of droplet impacts has been evaluated and the results are depicted in Fig. 5. Herein, the spreading diameter D_{spread} normalized by the maximum spreading diameter D_{max} is once provided in (a) as a function of the dimensionless (inertial) time $\tau = tu_0/D_0$ and once in (b) as a function in which the time is normalized by the capillary time,[49] $\tau_{cap} = t/\sqrt{\rho D_0^3/\gamma}$, where t is the time after impact. Each line represents the averaged values of one experimental set consisting of at least ten repetitions of the same impact parameters. During the spreading phase, while the inertial forces are dominant, all cases show a comparable behavior with a quickly increasing spreading diameter. This can be mainly explained by a large dynamic contact angle of approximately 180°, as stated before.[7] Using the dimensionless inertial time τ, the lines are clustering well during the spreading phase, supporting this statement.

The receding phase is strongly influenced by the different wetting behaviors of the solid–liquid combination and the capillary forces. Using the dimensionless capillary time τ_{cap} can show that the lines in Fig. 5(b) almost fully collapse to one line with respect to the liquid and wetting cases. The use of the dimensionless inertial time τ is rather unsuitable for this purpose. As can be seen in the graph, the full wetting cases of isopropanol slowly continue spreading after the dissipation of the kinetic energy. For water with an apparent contact angle of $\theta_{app} \approx 0°$, a very slight receding movement can be tracked, which leads to the assumption that the contact angle is very close to 0°, but not exactly. The lower the wettability of the surface, the more significant the receding movement, which can then promote a jet formation or even a (partial) rebound, as explained later in Sec. IV C. However, the receding rate is not only influenced by the surface wettability but also by the fluid surface tension and viscosity. Therefore, the receding rate of isopropanol is significantly lower than for water with comparable wetting behavior due to the combination of higher viscosity and lower surface tension. This is then the reason, why for all isopropanol cases no jet formation can be observed while for water cases several rebound events have been tracked.

After investigating the temporal evolution of the droplet spreading and receding, the maximum spreading diameter shall be evaluated while a detailed investigation of the receding behaviors shall be a subject of future work. Hereby, the maximum spreading diameter D_{max} is related to the impact diameter D_0. Figure 6(a) shows the mentioned spreading diameter relation vs the dimensionless inertial time τ at which this diameter is reached. It can be clearly seen that with increasing impact energy, which is here given in terms of impact height or wettability (θ_{app} is decreasing), the spreading diameter is increasing independently of the surface material onto which the droplet is impacting. The graph is not showing the full wetting isopropanol cases due to the continuous spreading as mentioned before. However, one can still determine the known behavior[10] that with increasing viscosity, which is the case for isopropanol in comparison to water, the maximum spreading diameter is decreasing.

For Figs. 6(b)–6(d), the dimensionless spreading diameters and dimensionless times of graph (a) are normalized with the spreading diameters of the full wetting cases as follows:

$$\tilde{D}_{max} = \frac{(D_{spread}/D_0)_{max}}{(D_{spread}/D_0)_{max}(\theta_{app} \approx 0°)}, \tag{12}$$

$$\tilde{\tau}_{max} = \frac{\tau((D_{spread}/D_0)_{max})}{\tau((D_{spread}/D_0)_{max}(\theta_{app} \approx 0°))}. \tag{13}$$

This normalization is independent of the selection of dimensional inertial and capillary time and can show how much less the droplet is spreading and how much shorter the spreading process is in comparison to the full wetting case. As depicted for all water cases in Fig. 6(b), the measurements are agglomerating onto one fitted line. Here, it can be clearly shown that the higher the apparent contact angle, the shorter and smaller the spreading magnitude (diameter and time). In more detail to the already mentioned finding, Fig. 6(c) is describing the spreading diameter decrease with respect to the wettability. With

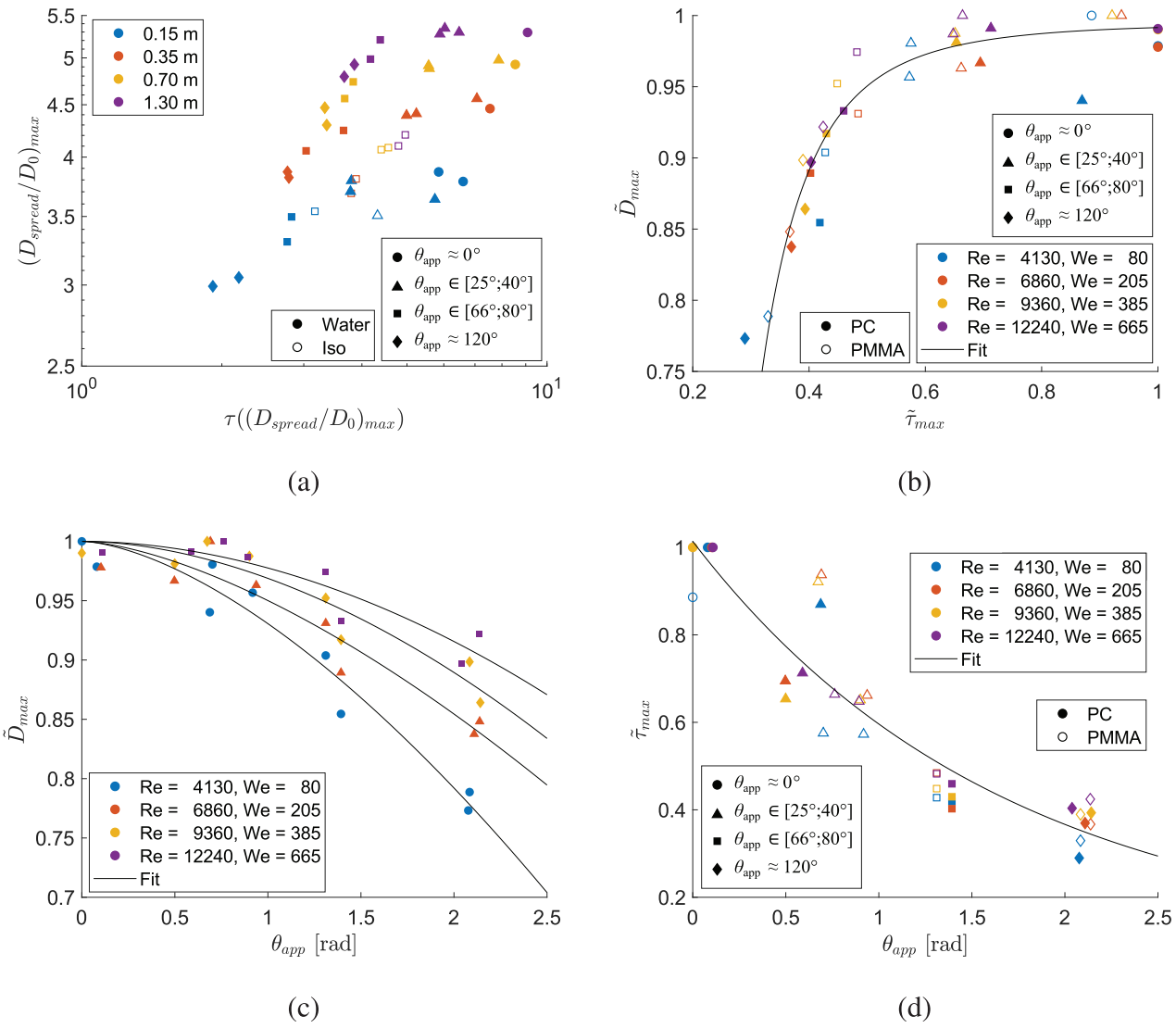

FIG. 6. (a) Dimensionless spreading diameter $[(D_{spread}/D_0)_{max}]$ over the dimensionless inertial time $\tau = tu_0/D_0$ at which the maximum spreading is reached in dependency of wetting behavior and impact energy (represented by the falling height); (b) maximum normalized dimensionless spreading diameter $\tilde{D}_{max}$ vs the corresponding time $\tilde{\tau}_{max}$ at which this diameter is reached showing the diameter decrease with increasing apparent contact angle θ_{app}; (c) maximum normalized dimensionless spreading diameter $\tilde{D}_{max}$ in dependency of the wetting behavior (θ_{app}) and the impact energy; and (d) $\tilde{D}_{max}$ over the apparent contact angle θ_{app} showing the influence of the impact energy and the wetting behavior.

increasing impact energy, the decrease in spreading diameter is becoming less significant, which is in agreement with Ref. 12 in which it is stated, that at a certain impact energy the influence of wettability is vanishing. The time when this maximum spreading diameter is reached is according to Fig. 6(d) almost independent of the impact energy itself, since the scatter points are agglomerating into the respective clusters for the different wetting behaviors which can be then fitted again.

C. Impact morphologies

After this overview, the comparison with empirical correlations and the evaluation of the droplet spreading, the obtained phenomena and their main features are described in detail.

Focusing on the lower impact energies tested ($We = 80$ for water and $We = 165$ for isopropanol), Fig. 7 shows a schematic of the most relevant results from the outcomes of droplet impingement onto a smooth dry surface with different materials and wettabilities. According to Pasandideh-Fard *et al.*,[12] wettability plays a negligible role for high impact energies but may be important for low impact velocities. In Fig. 7, there is a table for each fluid, distilled water, and isopropanol. The Reynolds and Weber numbers of the impacting droplets are also identified in the schemes. The apparent contact angles (θ_{app}) tested are indicated at the top of the tables and the different surface materials are divided: Lexan (PC) at the upper part and Plexiglas (PMMA) at the bottom part. These experiments correspond

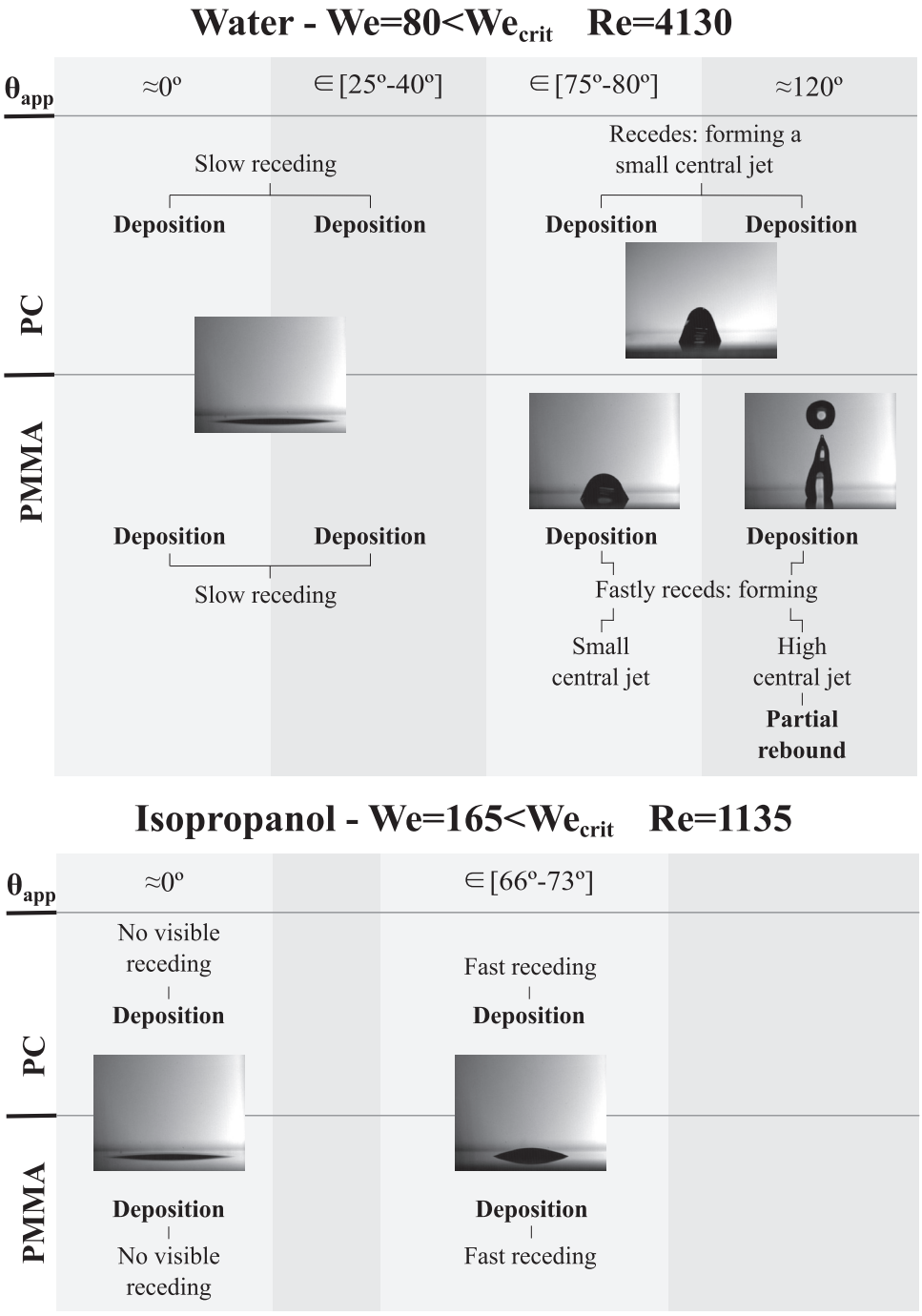

FIG. 7. Description of the morphology evolution depending on surface wettability and material for the lowest impact energy.

to a Weber number below the critical Weber number, We_{crit}, which defines the deposition/splashing limit, since only deposition was observed for all impact conditions tested. The impact upon the fully wettable surface results in a wide spreading with almost no receding, see Figs. 5 and 6. Slightly decreasing wettability ($\theta_{app} \in [20^\circ - 40^\circ]$), the spreading continues to be wide and there is a slow receding. Figure 8(a) shows the spreading of a water droplet impinging on a fully wettable Lexan surface from the three different perspectives (lateral, top, and bottom views). In all image sequences, the dimensionless inertial time is identified for each frame. Barely noticeable by the top and bottom views due to its size, a small air bubble is produced at the impact point. Bubble formation may happen due to different mechanisms.

Considering that the impact is on a cold surface, thus, below the liquid boiling point, a possible mechanism for the formation of bubbles is air entrapment at the liquid–solid interface during impact.[50] The gas between the impinging droplet and the solid surface forms a dimple and softens the impact. Thus, air is entrapped in the droplet by the dimple and a small bubble is formed since the air cannot escape.[51] This is the only air bubble on the liquid lamella that spreads over the surface until reaching the maximum spreading diameter. Inertia directs the liquid film to propagate radially, while the surface tension (interfacial energy) and the viscosity (dissipation of energy) are counteracting, which will consequently limit the maximum spreading diameter.[51] After reaching the maximum diameter, the liquid film remains on the surface and apparently does not recede inwards or recedes at a very slow velocity.

For water, where it is possible to find higher contact angles (partial wetting and nonwetting systems), the lamella recedes fast enough to allow the formation of a small central jet. Increasing even further the contact angle, so, in a nonwettable condition ($\theta_{app} \approx 120°$) for Plexiglas, the jet grows and in some cases breaks up ejecting a secondary droplet, the so-called partial rebound. The evolution of this phenomenon is displayed in Fig. 8(b). The liquid droplet spreads on the surface with a thick rim, reaches its maximum spreading diameter, and then recedes inwards forming a central jet that keeps growing upwards and breaks ejecting one or two secondary droplets. These droplets will ascend upwards until their ascendant velocity reaches $0\,m\,s^{-1}$ and starts their descendent movement toward the impact surface while impact velocity increases by gravity. When the droplets are ejected, the jet automatically decreases and balances until reaching an equilibrium position.

For Lexan, despite having the same wettability as Plexiglas for the nonwetting condition ($\theta_{app} \approx 120°$), the receding velocity seems to be rather slower, see Fig. 5, and the jet formed at the center is smaller, not allowing its breakup and consequent ejection of secondary droplets. This shows that changing surface material influences the morphology of the outcome even if we keep all the other parameters constant, including wettability. As mentioned previously, the surface wettability was changed through plasma treatments. In order to achieve a hydrophobic system, the samples have been treated using plasma polymerization. Despite both materials have the same wettability, the surface free energy and polarity of the surfaces have different values, which may play a role in the observed morphology.[26] Thus, the influence of these parameters will be investigated in more detail in future studies. From this analysis, it is possible to notice that increasing the contact angle increases the receding velocity. For fully wettable surfaces, the liquid stops after spreading and does not or only barely recedes. For impacts on nonwettable surfaces, the liquid recedes significantly faster forming a central jet which may disintegrate producing partial rebound.

Looking at the isopropanol results, the behavior is similar for the fully wettable condition, but for the partially wettable condition of $\theta_{app} \in [66° - 73°]$, there is no formation of a small central jet like it happened for the water impacts, probably due to the smaller surface tension. Here, the liquid film recedes inwards and stops when reaching equilibrium. Additionally, observing the maximum spreading diameter of a water droplet of similar impact conditions, it is easily acknowledged that isopropanol produces a smaller maximum spreading diameter. According to Mao *et al.*,[9] both viscosity and equilibrium contact angle play a significant role in the formation of rebound. Thus, isopropanol, which has a higher viscosity, will produce a smaller maximum spreading diameter, so it will have less energy available to recede toward the impact point and it consequently decreases the possibility of producing partial or total rebound. Additionally, isopropanol has a lower surface tension which might be considered as the restoring force. Consequently, high viscosity and low surface tension will both inhibit the tendency for rebound. For similar impact conditions, the receding for water seems to be faster than for isopropanol, see Fig. 5. However, the fact that the Reynolds number of the isopropanol droplets is considerably lower than the ones for water should not be forgotten. Nonetheless, the increase in receding velocity is noticeable while increasing the apparent contact angle and the tiny air bubble created at the impact point is present for all cases.

Moving on to the second set of impact energies tested, $We = 205$ for water which is below the splashing limit (We_{crit}), and $We = 400$ for isopropanol where splashing is observed, thus, above We_{crit}. Figure 9 shows a schematic of the phenomena observed during the impacts and their main characteristics. For water, splashing never occurred, only deposition was trackable. In addition, for the impact on nonwettable surfaces, partial rebound could be found. Here, the morphology is very similar to the first impact height. The receding velocity keeps increasing while decreasing wettability. Nonetheless, for the partial-wetting case, $\theta_{app} \in [75° - 80°]$, for both materials, there is a formation of a small central jet without its breakup, and for the nonwetting case, $\theta_{app} \approx 120°$, partial rebound was observed in some cases for both materials. Thus, considering the surface wettability influence and its role in the receding behavior, the impact energy was large enough to allow central jet breakup and ejection of one or two secondary droplets for the impact of a single droplet upon a nonwettable Lexan surface.

Regarding the impact of the isopropanol droplets, as already mentioned, splashing was observed for both wettabilities on the impact with both materials. However, for the fully wettable surfaces, there is no visible receding and for the partial-wettable experiments, $\theta_{app} \in [66° - 73°]$, the receding is quite fast. Confirming that receding velocity increases while increasing the equilibrium contact angle. Figure 8(c) shows the evolution of splashing on the impact of an isopropanol droplet onto a partially wettable Plexiglas surface. Similar to the previous results, a tiny air bubble entrapped inside the liquid film is created at the moment of impact at the impact point. As touching the surface, prompt splash is immediately produced by the ejection of tiny jets. These jets evolve creating a liquid crown sheet that continues its growth in diameter and height producing secondary atomization. The crown breaks and the liquid lamella remains on the surface, receding inwards until reaching an equilibrium position.

The third set of impact energies tested shows similar results to the previous one, and their outcomes are displayed in Fig. 10. The impact of a water droplet with $We = 385$ does not produce secondary droplets except for the higher contact angles, where partial rebound occurs and a rebound droplet is ejected. A novelty resides in the production of fingering on the spreading of the liquid droplet caused by instabilities on the advancing rim. Additionally, on the impact of water droplets onto the nonwettable Plexiglas surface, a new phenomenon was observed, complete rebound, Fig. 8(d). The liquid film spreads on the surface showing a fingering pattern until reaching its maximum

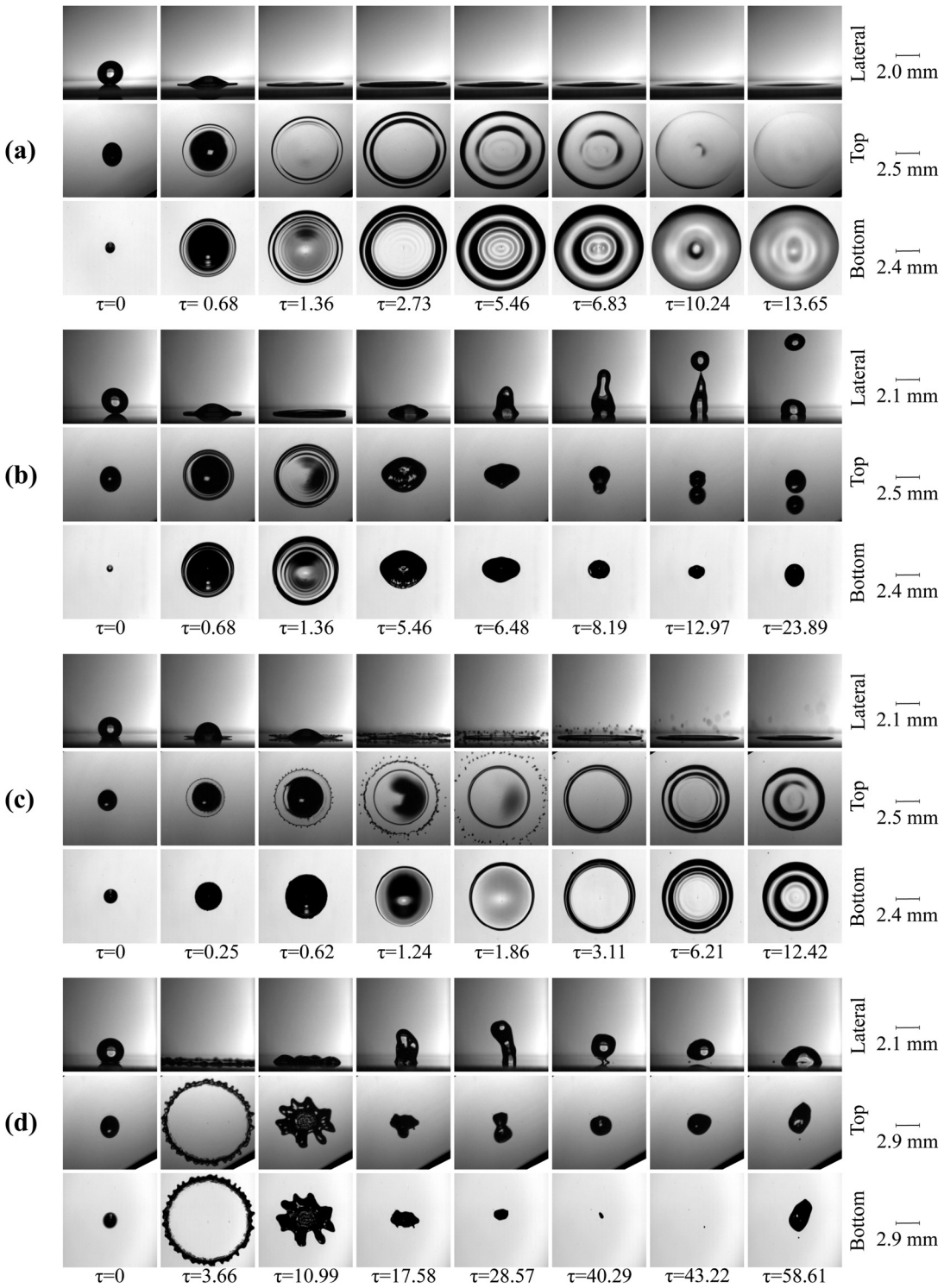

FIG. 8. Sequence of images showing the phenomena obtained by the lateral, top, and bottom views: (a) spreading of a water droplet impinging onto a fully wettable Lexan surface ($\theta_{app} \approx 0^\circ$) for $We = 80$ and $Re = 4130$; (b) partial rebound of a water droplet impinging onto a nonwettable Plexiglas surface ($\theta_{app} \approx 120^\circ$) for $We = 80$ and $Re = 4130$; (c) splashing of an isopropanol droplet impinging onto a partially wettable Plexiglas surface ($\theta_{app} \approx 70^\circ$) for $We = 400$ and $Re = 1745$; and (d) complete rebound of a water droplet impinging onto a nonwettable Plexiglas surface ($\theta_{app} \approx 120^\circ$) for $We = 385$ and $Re = 9360$.

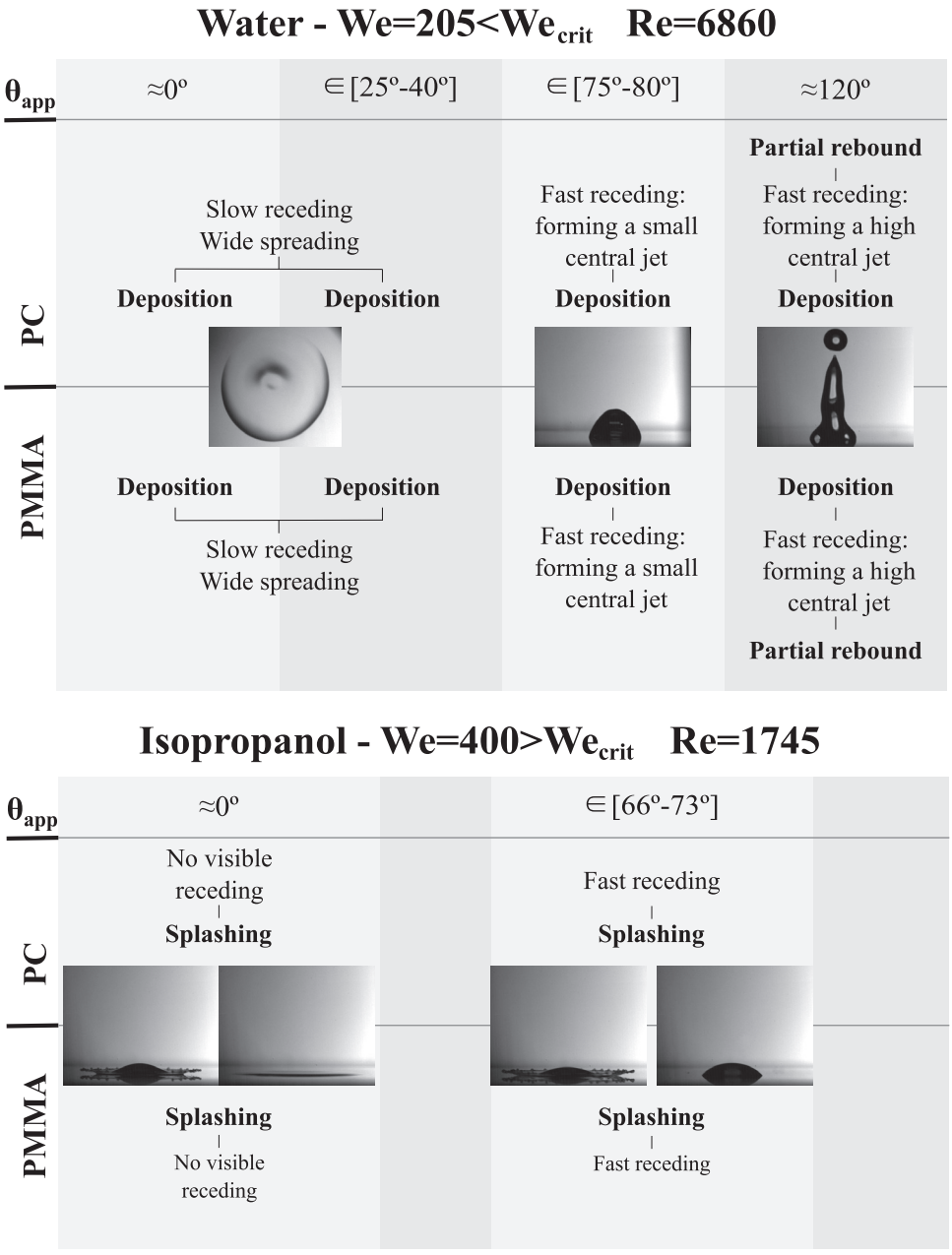

FIG. 9. Morphology evolution depending on surface wettability for the second impact energy tested.

spreading diameter and then quickly recedes inwards forming a high central jet. For two out of ten experiments made, the jet grows upwards and becomes thicker at the top while it becomes thinner at the bottom part of the jet. The jet starts decreasing its height while becomes thinner at the bottom part, assuming a droplet-like shape, $\tau = 40.29$. The liquid film totally detaches from the surface originating complete rebound, $\tau = 43.22$. After a short period of time, the droplet impacts the hydrophobic surface again at a low impact energy.

Regarding the outcomes of the isopropanol droplet impact at $We = 715$, splashing was observed for all cases, with the production of both prompt and crown splash. The major difference compared to the lower impact energy regards the magnitude of splashing, producing more secondary droplets.

Finally, to enrich the study, high impact energies were also tested to assess their influence on the observed morphology. Surface wettability plays a relevant role in the spreading, receding, and rebound dynamics. However, this influence can be diminished or suppressed by the impact conditions.[52] Droplet impact velocity, u_0, strongly affects spreading and splashing regimes due to the transfer of kinetic energy after impact. The scheme in Fig. 11 shows the phenomena obtained and their main characteristics.

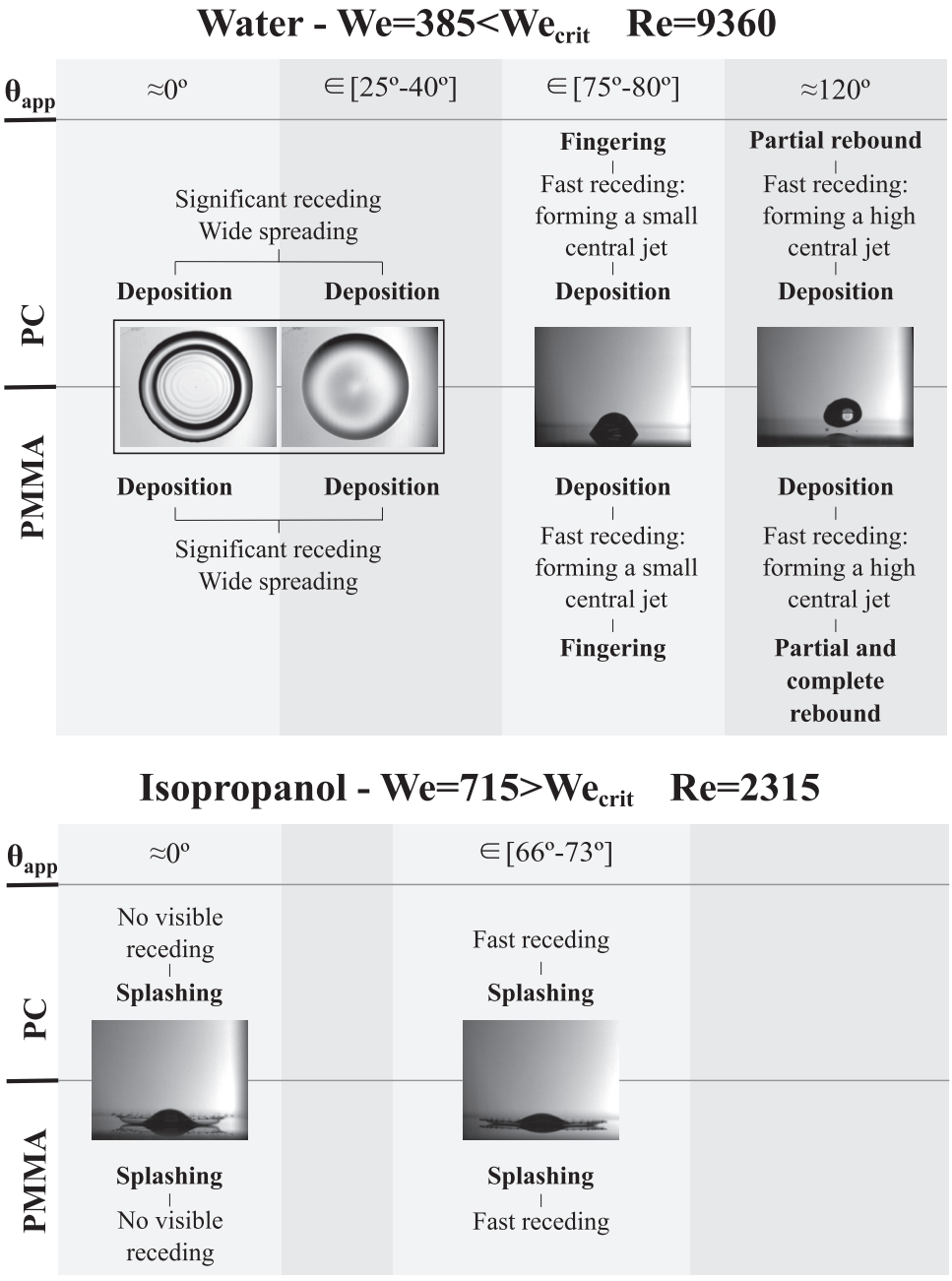

FIG. 10. Morphology evolution depending on surface wettability for the third impact energy tested.

Focusing on distilled water, the impact of a droplet with $We = 665$ on the surfaces with lower apparent contact angles originated deposition but in this case with a wider spreading and with a significant receding due to the increase in kinetic energy. Additionally, the rim assumed an initial fingering-like pattern. For the impact on the partially wettable surface, $\theta_{app} \in [75^\circ - 80^\circ]$, only deposition was observed but with a significant fingering pattern at the beginning of spreading. Similar to lower impact energies, the liquid lamella quickly recedes and forms a small central jet. The spreading seems to be wider, so probably a significant part of the droplet kinetic energy is spent on the spreading phase. On the impact onto the nonwettable surface, $\theta_{app} \approx 120^\circ$, the liquid droplet has a fast and wide spreading and a fast receding originating receding breakup. However, even with some receding breakup, there are some cases of partial rebound on the impact with the Plexiglas surface.

Finally, during the impact of isopropanol droplets at high impact energy, $We = 1165$, splashing is observed with higher magnitude than the lower impact energies, e.g., observable in more secondary droplets. Again, the receding velocity for less wettable surfaces was higher than on the fully wettable ones.

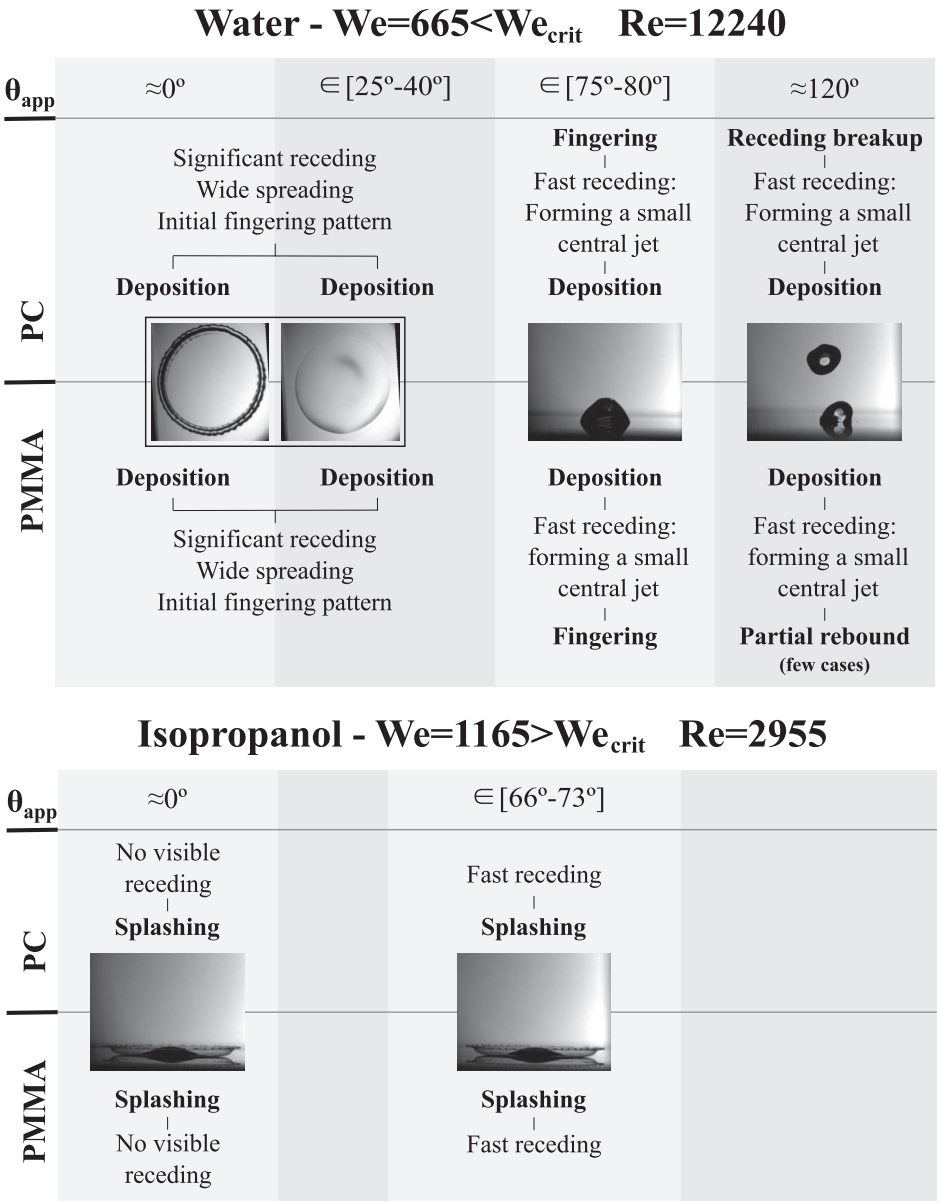

FIG. 11. Morphology evolution depending on surface wettability for the highest impact energy.

V. DISCUSSION AND OUTLOOK

Wettability is an important and challenging parameter in the study of droplet impingement. The goal of this work was to assess the influence of wettability on the impact of single droplets onto a dry smooth surface and to identify the originated phenomena and their characteristics. To achieve that, distilled water and isopropanol were used as fluids impinging on Lexan and Plexiglas surfaces with different wettability behaviors. The apparent contact angles between the fluid and the surface were changed through plasma treatments obtaining up to four different wettability behaviors. Moreover, different impact energies were tested to investigate their influence on the outcomes, the spreading and receding behavior. A meticulous experimental facility was developed to perform these experiments and provided three perspectives of the phenomena observation (lateral, top, and bottom views). The bottom view in internal total reflection configuration, less reported in the literature, helped us to understand important features of the phenomena morphology.

The phenomena obtained were categorized into three different regimes: deposition, splashing, and rebound. The correlation developed by Vander Wal *et al.*[46] has a validity range that can be applied to our results and provides good agreement between the predicted and the obtained regimes.

The first impact energy tested, $We = 80$ for distilled water and $We = 165$ for isopropanol, is below the splashing limit, We_{crit}. Only deposition was observed for these energies for all sets of impact conditions. By normalizing droplet spreading diameters, it was noticeable

that with decreasing wettability, the receding rate is increasing. Additionally, the maximum spreading diameter is decreasing as well as the spreading duration. The liquid stops and barely recedes while impacting on a fully wettable surface. On the other hand, on the impact with a nonwettable surface, it quickly recedes forming a central jet which may break up and produce partial rebound. The water droplet impact on hydrophobic surfaces, despite having the same impact conditions, originates a different outcome depending on the surface material. That fact could be related to differences in the polarity and free surface energy of the samples due to the plasma treatment. This fact will be investigated in future studies.

Isopropanol, which has a higher viscosity, shows a smaller maximum spreading diameter than distilled water. Increasing the impact energy to $We = 400$ produces splashing. So, the critical deposition/splashing limit is located within $165 < We < 400$.

Increasing the impact energy increased the probability to obtain partial rebound on the water droplet impact with hydrophobic surfaces. Some cases of complete rebound were observed on the water droplet impact at $We = 385$ on a nonwettable Plexiglas surface. Increasing the impact energy even further allows the formation of a wide spreading on the surface. This leads to a thin enough lamella which is going to break up during the receding. Due to the receding breakup, the central jet formed is smaller and partial rebound is inhibited.

ACKNOWLEDGMENTS

The authors kindly acknowledge the financial support of this work by the Deutsche Forschungsgemeinschaft (DFG) in the frame of the International Research Training Group "Droplet Interaction Technologies" (*GRK 2160: DROPIT*) under the Project No. 270852890. Additionally, the authors would like to acknowledge the support of Fundação para a Ciência e a Tecnologia (FCT) through the Ph.D. scholarship SFRH/BD/140009/2018 and the Project No. UIDB/50022/2020.

DATA AVAILABILITY

The data that support the findings of this study are available from the corresponding author upon reasonable request.

REFERENCES

[1]A. Yarin, I. Roisman, and C. Tropea, *Collision Phenomena in Liquids and Solids* (Cambridge University Press, 2017).
[2]R. Rioboo, C. Tropea, and M. Marengo, "Outcomes from a drop impact on solid surfaces," Atomization Sprays **11**, 12–165 (2001).
[3]R. Blossey, "Self-cleaning surfaces—virtual realities," Nat. Mater. **2**, 301–306 (2003).
[4]B. S. Yilbas, A. Al-Sharafi, and, H. Ali, "Application of water droplet for self-cleaning of surfaces," in *Self-Cleaning of Surfaces and Water Droplet Mobility*, edited by B. S. Yilbas, A. Al-Sharafi, and H. Ali (Elsevier, 2019), Chap. 7, pp. 375–421.
[5]M. Zhang, S. Feng, L. Wang, and Y. Zheng, "Lotus effect in wetting and self-cleaning," Biotribology **5**, 31–43 (2016).
[6]T. Young, "III. An essay on the cohesion of fluids," Philos. Trans. R. Soc. London **95**, 65–87 (1805).
[7]V. E. B. Dussan, "The moving contact line: The slip boundary condition," J. Fluid Mech. **77**, 665–684 (1976).
[8]G. Elliott and A. Riddiford, "Dynamic contact angles: I. The effect of impressed motion," J. Colloid Interface Sci. **23**, 389–398 (1967).
[9]T. Mao, D. C. S. Kuhn, and H. Tran, "Spread and rebound of liquid droplets upon impact on flat surfaces," AIChE J. **43**, 2169–2179 (1997).
[10]R. Rioboo, M. Marengo, and C. Tropea, "Time evolution of liquid drop impact onto solid, dry surfaces," Exp. Fluids **33**, 112–124 (2002).
[11]A. S. Moita and A. L. N. Moreira, "Influence of surface properties on the dynamic behavior of impacting droplets," in *Proceedings of the 9th ICLASS—Europe* (Institute for Liquid Atomization and Spray Systems, Sorrento, Italy, 2003).
[12]M. Pasandideh-Fard, Y. M. Qiao, S. Chandra, and J. Mostaghimi, "Capillary effects during droplet impact on a solid surface," Phys. Fluids **8**, 650–659 (1996).
[13]C. Antonini, A. Amirfazli, and M. Marengo, "Drop impact and wettability: From hydrophilic to superhydrophobic surfaces," Phys. Fluids **24**, 102104 (2012).
[14]M. A. Quetzeri-Santiago, K. Yokoi, A. A. Castrejón-Pita, and J. R. Castrejón-Pita, "Role of the dynamic contact angle on splashing," Phys. Rev. Lett. **122**, 228001 (2019).
[15]A. Latka, A. M. P. Boelens, S. R. Nagel, and J. J. de Pablo, "Drop splashing is independent of substrate wetting," Phys. Fluids **30**, 022105 (2018).
[16]A. Karl, J. Wolber, and A. Frohn "Interaction of droplet groups with hot walls above the Leidenfrost-temperature," in *Proceedings of the 13th International Conference on Liquid Atomization and Spray Systems (1997)*, Vol. 13, pp. 458–464.
[17]N. Roth, A. Karl, and A. Frohn, "Observation of liquid-wall contact during droplet impact," in Proceedings of the 14th International Conference on Liquid Atomization and Spray Systems (1998), Vol. 14, pp. 103–107.
[18]N. R. Arnold Frohn, in *Dynamics of Droplets* (Springer, Berlin/Heidelberg, 2000).
[19]M. A. van Limbeek, M. Shirota, P. Sleutel, C. Sun, A. Prosperetti, and D. Lohse, "Vapour cooling of poorly conducting hot substrates increases the dynamic Leidenfrost temperature," Int. J. Heat Mass Transfer **97**, 101–109 (2016).
[20]A. Marmur, C. Della Volpe, S. Siboni, A. Amirfazli, and J. W. Drelich, "Contact angles and wettability: Towards common and accurate terminology," Surf. Innovations **5**, 3–8 (2017).
[21]D. K. Owens and R. C. Wendt, "Estimation of the surface free energy of polymers," J. Appl. Polym. Sci. **13**, 1741–1747 (1969).
[22]W. Rabel, "Einige Aspekte der Benetzungstheorie und ihre Anwendung auf die Untersuchung und Veränderung der Oberflächeneigenschaften von Polymeren," Farbe Lacke **77**, 997–1005 (1971).
[23]D. H. Kaelble, "Dispersion-polar surface tension properties of organic solids," J. Adhes. **2**, 66–81 (1970).
[24]F. M. Fowkes, "Attractive forces at interfaces," Ind. Eng. Chem. **56**, 40–52 (1964).
[25]G. Ström, M. Fredriksson, and P. Stenius, "Contact angles, work of adhesion, and interfacial tensions at a dissolving hydrocarbon surface," J. Colloid Interface Sci. **119**, 352–361 (1987).
[26]DataPhysics Instruments GmbH, https://www.dataphysics-instruments.com/Downloads/Surface-Tensions-Energies.pdf for "Surface tensions/energies" (2018).
[27]M. Greiveldinger and M. E. Shanahan, "A critique of the mathematical coherence of acid/base interfacial free energy theory," J. Colloid Interface Sci. **215**, 170–178 (1999).
[28]W. Wagner and A. Pruß, "The IAPWS formulation 1995 for the thermodynamic properties of ordinary water substance for general and scientific use," J. Phys. Chem. Ref. Data **31**, 387–535 (2002).
[29]J. R. Rumble, "Density rho at the temperature in c indicated by superscript," *CRC Handbook of Chemistry and Physics* (CRC Press, Taylor & Francis Group, 2019).
[30]M. L. Huber, R. A. Perkins, A. Laesecke, D. G. Friend, J. V. Sengers, M. J. Assael, I. N. Metaxa, E. Vogel, R. Mareš, and K. Miyagawa, "New international formulation for the viscosity of H_2O," J. Phys. Chem. Ref. Data **38**, 101–125 (2009).
[31]J. R. Rumble, "Surface tension at various temperatures," *CRC Handbook of Chemistry and Physics* (CRC Press, Taylor & Francis Group, 2019).
[32]IAPWS, "Revised release on surface tension of ordinary water substance," Report No. R1-76 (International Association for the Properties of Water and Steam, 2014).

[33]J. R. Rumble, "Viscosity of liquids as a function of temperature," *CRC Handbook of Chemistry and Physics* (CRC Press, Taylor & Francis Group, 2019).
[34]A. Yarin, "Drop impact dynamics: Splashing, spreading, receding, bouncing…," Annu. Rev. Fluid Mech. **38**, 159–192 (2006).
[35]M. Marengo, C. Antonini, I. V. Roisman, and C. Tropea, "Drop collisions with simple and complex surfaces," Curr. Opin. Colloid Interface Sci. **16**, 292–302 (2011).
[36]Y. D. Chashechkin, "Visualization of the fine perturbation structure of a liquid surface by flows induced by a drop impact," Fluid Dyn. **54**, 919–926 (2019).
[37]D. Ribeiro, M. O. Panão, J. M. Barata, and, and A. R. Silva, "Morphology of bubble formation on droplet impact upon thin liquid layers," in *AIAA Scitech 2020 Forum* (American Institute of Aeronautics and Astronautics, Orlando, FL, 2020).
[38]Optik, edited by E. Hecht, in *Optik*, 3rd ed. (Addison-Wesley, Bonn, 1994), pp. 717.
[39]Schott AG, "Optical Glass – Data Sheets," Report (2017), available at https://www.schott.com/d/advanced_optics/ac85c64c-60a0-4113-a9df-23ee1be20428/1.17/schott-optical-glass-collection-datasheets-english-may-2019.pdf.
[40]P. E. Ciddor, "Refractive index of air: new equations for the visible and near infrared," Appl. Opt. **35**, 1566–1573 (1996).
[41]Photron, Fastcam SA-X2—Dataseheet, rev# 17.03.03 ed., 2017.
[42]H. Zhang, X. Zhang, X. Yi, F. He, F. Niu, and P. Hao, "Effect of wettability on droplet impact: Spreading and splashing," Exp. Therm. Fluid Sci. **124**, 110369 (2021).
[43]A. Fridman, *Plasma Chemistry* (Cambridge University Press, 2008).
[44]L. P. Yarin, *The Pi-Theorem: Applications to Fluid Mechanics and Heat and Mass Transfer*, Experimental Fluid Mechanics Vol. 1 (Springer-Verlag GmbH, Berlin, 2012).
[45]N. Otsu, "A threshold selection method from gray-level histograms," IEEE Trans. Syst., Man, Cybern. **9**, 62–66 (1979).
[46]R. L. Vander Wal, G. M. Berger, and S. D. Mozes, "The splash/non-splash boundary upon a dry surface and thin fluid film," Exp. Fluids **40**, 53–59 (2006).
[47]C. Bai and A. Gosman, "Development of methodology for spray impingement simulation," SAE Trans. **104**, 550–568 (1995).
[48]C. Mundo, M. Sommerfeld, and C. Tropea, "Droplet-wall collisions: Experimental studies of the deformation and breakup process," Int. J. Multiphase Flow **21**, 151–173 (1995).
[49]Y. Zhu, H.-R. Liu, K. Mu, P. Gao, H. Ding, and X.-Y. Lu, "Dynamics of drop impact onto a solid sphere: preading and retraction," J. Fluid Mech. **824**, R3 (2017).
[50]S. Chandra and C. T. Avedisian, "On the collision of a droplet with a solid surface," Proc. R. Soc. London, Ser. A **432**, 13–41 (1991).
[51]C. W. Visser, P. E. Frommhold, S. Wildeman, R. Mettin, D. Lohse, and C. Sun, "Dynamics of high-speed micro-drop impact: numerical simulations and experiments at frame-to-frame times below 100 ns," Soft Matter **11**, 1708–1722 (2015).
[52]S. Moghtadernejad, C. Lee, and M. Jadidi, "An introduction of droplet impact dynamics to engineering students," Fluids **5**(3), 107 (2020).